

The Interplay between Strain, Sn Content, and Temperature on Spatially Dependent Bandgap in $\text{Ge}_{1-x}\text{Sn}_x$ Microdisks

Ignatii Zaitsev,* Agnieszka Anna Corley-Wiciak,* Cedric Corley-Wiciak, Marvin Hartwig Zoellner, Carsten Richter, Edoardo Zatterin, Michele Virgilio, Beatriz Martín-García, Davide Spirito, and Costanza Lucia Manganelli*

Germanium–tin (GeSn) microdisks are promising structures for complementary metal–oxide–semiconductor-compatible lasing. Their emission properties depend on Sn concentration, strain, and operating temperature. Critically, the band structure of the alloy varies along the disk due to different lattice deformations associated with mechanical constraints. An experimental and numerical study of $\text{Ge}_{1-x}\text{Sn}_x$ microdisk with Sn concentration between 8.5 and 14 at% is reported. Combining finite element method calculations, micro-Raman and X-ray diffraction spectroscopy enables a comprehensive understanding of mechanical deformation, where computational predictions are experimentally validated, leading to a robust model and insight into the strain landscape. Through micro-photoluminescence experiments, the temperature dependence of the bandgap of $\text{Ge}_{1-x}\text{Sn}_x$ is parametrized using the Varshni formula with respect to strain and Sn content. These results are the input for spatially dependent band structure calculations based on deformation potential theory. It is observed that Sn content and temperature have comparable effects on the bandgap, yielding a decrease of more than 20 meV for an increase of 1 at% or 100 K, respectively. The impact of the strain gradient is also analyzed. These findings correlate structural properties to emission wavelength and spectral width of microdisk lasers, thus demonstrating the importance of material-related consideration on the design of optoelectronic microstructures.

1. Introduction

An all-in-one complementary metal–oxide–semiconductor chip that contains laser sources, photodetectors, waveguides, and modulators is one of the most crucial milestones of silicon photonics, envisioning faster, more compact, and more efficient optoelectronic devices. The biggest challenge in achieving this goal is a fully integrated laser source on silicon.^[1–4]

One of the research paths toward this aim focuses on Ge and its alloys, such as germanium–tin ($\text{Ge}_{1-x}\text{Sn}_x$) and silicon–germanium–tin.^[5] The composition of the material can be adjusted to cover a wide range of infrared wavelengths, from 1.6 to 5 μm .^[6–8] With increase of Sn concentration in the alloy, the energy separation between the Γ and L valleys of the conduction band increases, and, above 8%, a transition from indirect to direct bandgap is observed in unstrained samples.^[9] In addition to the higher radiative recombination probability, this results in a larger population of electrons in the Γ -valley at a given

I. Zaitsev, A. A. Corley-Wiciak, C. Corley-Wiciak, M. H. Zoellner, D. Spirito, C. L. Manganelli
IHP–Leibniz-Institut für Innovative Mikroelektronik
Im Technologiepark 25, 15236 Frankfurt (Oder), Germany
E-mail: zaitsev@ihp-microelectronics.com;
wiciak@ihp-microelectronics.com;
manganelli@ihp-microelectronics.com

A. A. Corley-Wiciak
RWTH Aachen University
Templergraben 55, 52062 Aachen, Germany

 The ORCID identification number(s) for the author(s) of this article can be found under <https://doi.org/10.1002/pssr.202300348>.

© 2023 The Authors. physica status solidi (RRL) Rapid Research Letters published by Wiley-VCH GmbH. This is an open access article under the terms of the Creative Commons Attribution-NonCommercial-NoDerivs License, which permits use and distribution in any medium, provided the original work is properly cited, the use is non-commercial and no modifications or adaptations are made.

DOI: 10.1002/pssr.202300348

C. Richter
IKZ – Leibniz -Institut für Kristallzüchtung
Max-Born-Straße 2, D-12489 Berlin, Germany

E. Zatterin
ESRF – European Synchrotron Radiation Facility
71, avenue des Martyrs, CS 40220, 38043 Grenoble Cedex 9, France

M. Virgilio
Dipartimento di Fisica “Enrico Fermi”
Università di Pisa
Largo Bruno Pontecorvo 3, 56127 Pisa, Italy

B. Martín-García
CIC nanoGUNE BRTA Tolosa Hiribidea
76, Basque Country, 20018 Donostia-San Sebastián, Spain

B. Martín-García
IKERBASQUE, Basque Foundation for Science
Basque Country, 48009 Bilbao, Spain

temperature and reduces electron intervalley scattering between the Γ and L valleys.^[10,11]

Furthermore, mechanical deformations combined with tuned Sn content allow to control of both valence and conduction band edges and enhance carrier mobility^[12] and direct optical emission.^[13–15] The development and improvement in the performance of $\text{Ge}_{1-x}\text{Sn}_x$ -based lasers was obtained by acting on strain and Sn content since the first proof-of-principle in 2015^[16] and reaching operating temperature of 130 K,^[12] 180 K,^[17] and 230 K^[18] for both continuous-wave and pulsing modes of optically pumped lasers, with the lasing threshold as low as 0.8 kW cm^{-2} .^[13] Recent activities^[11] have demonstrated room-temperature lasing for optically pumped lasers in pulsed mode, while the state-of-the-art for electrically pumped lasers has achieved milestones up to 90 K.^[19,20] Several efforts have been also devoted to study laser designs based on Fabry Perot cavities,^[16] photonic crystals,^[18,21] or microbridges.^[6] Nonetheless, the fine-tuning of alloys and microstructures toward specific applications requires a thorough understanding of the contribution of individual parameter to the $\text{Ge}_{1-x}\text{Sn}_x$ band structure, which essentially depends on the interplay between Sn content and thermomechanical properties of the devices operating under different temperatures.

Moreover, a nonuniform distribution of lattice strain can be present in microstructures, affecting device performance and optical properties. Its analysis requires a complete calculation of the mechanical deformation and the band structure that spans the whole volume of the microdevice, which is the topic of this work.

The mechanical deformation of the $\text{Ge}_{1-x}\text{Sn}_x$ layers stems from their epitaxial growth on a plastically relaxed Ge virtual substrate (VS). The addition of Sn increases the size of the unit cell compared to Ge. Therefore, the $\text{Ge}_{1-x}\text{Sn}_x$ is generally under compressive strain, which decreases the directness of the bandgap.^[22] This strain may be released by plastic relaxation of the $\text{Ge}_{1-x}\text{Sn}_x$ epilayer, but this leads to the generation of a high density of dislocations, which have an adverse effect on device performance.^[23] One approach to overcome this limitation is the fabrication of suspended or free-standing microstructures from the $\text{Ge}_{1-x}\text{Sn}_x$ epilayers, which can relax elastically, yielding unstrained and defect-free $\text{Ge}_{1-x}\text{Sn}_x$ suitable for optoelectronic applications.^[24] A good example is $\text{Ge}_{1-x}\text{Sn}_x$ microdisks, obtained by selective etching of the Ge substrate, to have an elastically relaxed suspended $\text{Ge}_{1-x}\text{Sn}_x$ rim. Thus, we study in detail a series of $\text{Ge}_{1-x}\text{Sn}_x$ microdisks with a toolkit of complementary experimental and simulation techniques. We investigate the spatial strain distribution by micro-Raman spectroscopy and finite element method (FEM) calculations in COMSOL Multiphysics. Next, we provide a parametrization model of the temperature-dependent bandgap, analyzing the interplay between strain, temperature, and Sn content. Finally, we offer a fully integrated calculation platform for evaluating strain-, temperature- and, most importantly, Sn content-dependent bandgap into a FEM modeling. This modeling and parameterization of the optical properties of realistic $\text{Ge}_{1-x}\text{Sn}_x$ -based microdevices can be applied to arbitrary device designs, providing a guide for the optimization of their performance.

2. Experimental Section

2.1. Samples

We selected a series of samples that differ in their Sn content and thickness within the capability of epitaxial deposition. In this way, we can explore a range of composition and mechanical configuration for a material that has the high quality required for photonics application.

Microdisks were fabricated from epitaxial $\text{Ge}_{1-x}\text{Sn}_x/\text{Ge}/\text{Si}$ wafers as described in ref. [12]. The layers are deposited by chemical vapor deposition.^[12] The thickness of the Ge VS is 3 μm , while for $\text{Ge}_{1-x}\text{Sn}_x$ layers it varies between 220 and 800 nm. The nominal Sn content is between 8.5 and 14 at%, as listed in **Table 1**. On each wafer, arrays of microdisks are structured by e-beam lithography and selective etching.^[12] Each disk thus consists of a plastically relaxed Ge pedestal on a Si (001) substrate, which supports a $\text{Ge}_{1-x}\text{Sn}_x$ disk with a suspended rim. The disk diameter is defined by the lithographic process, and varies in the range 20–140 μm , while the suspended rim extends always by 5 μm , controlled by the etching process. A scanning electron microscopy image of a disk of 20 μm radius is shown in the inset of **Figure 1a**.

In Table 1, also the strain values measured by micro-Raman spectroscopy in the central part of the microdisks are reported. These values are similar to the ones measured in the bulk samples and show the impact of not only Sn content and plastic relaxation, but also thickness on the resulting strain behavior.

2.2. Raman

Raman spectroscopy provides information about strain and composition in $\text{Ge}_{1-x}\text{Sn}_x$ microstructures.^[15,25] Raman studies at room temperature were carried out using a Renishaw inVia system, with a spectrometer equipped with a 2400 grooves mm^{-1} grating. The system was set up to work in a backscattering mode, and a 100 \times magnification objective was employed. An excitation wavelength of 532 nm was used, corresponding to a sampling depth of about 10 nm from the sample surface. For low-temperature measurements, we employed a Renishaw inVia Qontor system equipped with a vacuum chamber (10^{-6} hPa) Linkam HFS350EV-PB4, with liquid nitrogen cooling (temperature range -193 to 350 $^{\circ}\text{C}$), with a 633 nm laser excitation, a 2400 grooves mm^{-1} grating, and a 50 \times long working distance objective. The lateral resolution corresponds to the

Table 1. List of the $\text{Ge}_{1-x}\text{Sn}_x$ samples.

Sample	Sn content [%]	Thickness of $\text{Ge}_{1-x}\text{Sn}_x$ [nm]	Strain in the center (ϵ_b) [%]
Sn8.5	8.5	880	−0.37
Sn10_thin	10	220	−0.46
Sn10_thick	10	710	−0.37
Sn12.5_thin	12.5	350	−0.55
Sn12.5_thick	12.5	414	−0.5
Sn14	14	350	−0.55

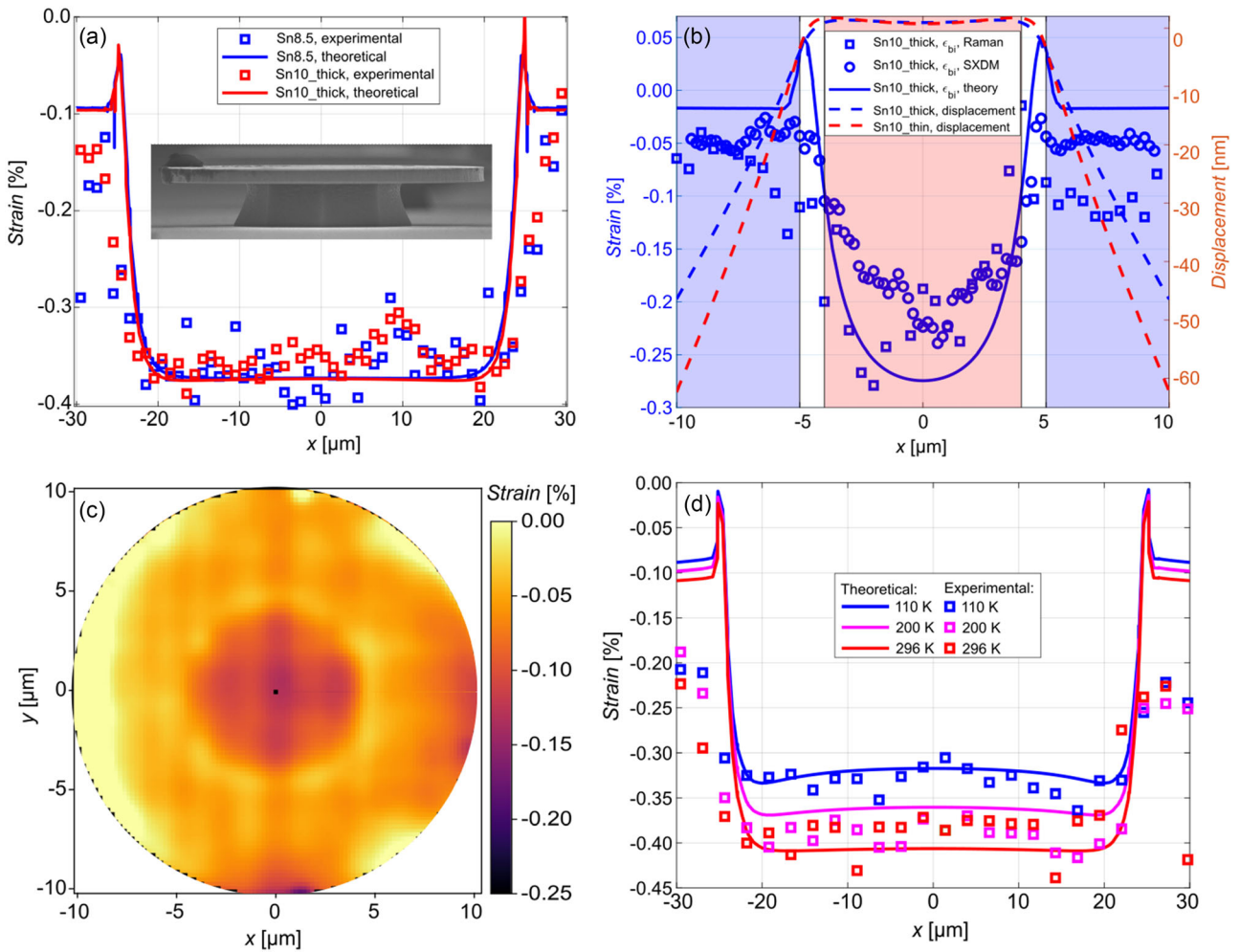


Figure 1. a) Biaxial strain profiles along the diameters of 60 μm disks on sample Sn8.5 (8.5% Sn, 880 nm, blue symbols and line) and Sn10_thick (10% Sn, 710 nm, red symbols and line) at room temperature. b) Biaxial strain profile along the diameter of a smaller (20 μm wide) disk on sample Sn10_thick with the center and rim areas marked out. Displacement is reported as dashed lines, right-hand axis. c) SXDM map of biaxial strain in a sample Sn12.5_thick (8.5% Sn, 20 μm wide, 414 nm thick). d) Strain profiles along the diameters of a 60 μm wide Sn10_thick disk at different temperatures.

spot size of the laser beam around 500 nm. Raman spectra maps and profiles along the diameter of the disks were taken with the step size of 500 nm. From the peak position of the Ge–Ge mode, the strain values were determined with the following formula:

$$\omega = \omega_0 + ax + b\epsilon_{\text{bi}} \quad (1)$$

where ω_0 is a characteristic wavenumber; a and b are, respectively, content and strain coefficients that amount to $\omega_0 = 301.1 \text{ cm}^{-1}$, $a = -92 \text{ cm}^{-1}$, $b = -550 \text{ cm}^{-1}$.^[26] x is the Sn concentration; $\epsilon_{\text{bi}} = \frac{\epsilon_{xx} + \epsilon_{yy}}{2}$ is the local in-plane lattice strain. For samples Sn12.5_thick and Sn10_thick, the strain values measured by Raman spectroscopy were confirmed by nanobeam scanning X-ray diffraction microscopy (SXDM).

2.3. SXDM

SXDM^[27] was performed at the beamline ID01/ESRF with an X-ray beam focused down to <200 nm. Strain maps were calculated following the measurement and analysis procedures previously developed.^[28]

2.4. Photoluminescence

Temperature-dependent photoluminescence (PL) was measured between 80 and 270 K, using a 1064 nm laser for excitation. Focusing was achieved by an objective with 50 \times magnification and a numerical aperture of 0.65. PL emittance spectra of the sample were taken in backscattering geometry with a 600 lines/mm grating and an extended indium gallium arsenide (InGaAs) photodiode array acting as the detector. For cooling

and temperature control, the sample was placed in a Linkam cryostat with a temperature accuracy of 5 K.

2.5. FEM Calculations

3D FEM simulations with the Solid Mechanics module of COMSOL Multiphysics allow us to predict the behavior of the strain profile.

The mechanical deformation is evaluated according to Hooke's law^[14] in a 3D description to offer a complete overview of all the strain field components.

$$\sigma_{ij} = C_{ijkl}\epsilon_{kl} \quad (2)$$

Here, σ_{ij} is the stress tensor, ϵ_{kl} is the strain tensor, and C_{ijkl} is the stiffness tensor.

The lattice strain in the central part of the disk is treated as biaxial, which is an approximation assuming its shape is ideally circular and governed by the lattice mismatch between the Ge pedestal and the $\text{Ge}_{1-x}\text{Sn}_x$ layer up to the mismatch-dependent "critical thickness."^[29] Upon exceeding the critical thickness, the $\text{Ge}_{1-x}\text{Sn}_x$ layer may undergo plastic relaxation to some degree, depending on growth conditions^[30] by the formation of misfit dislocations, and release the lattice strain. Therefore, the strain at the center of each disk is different, dependent on the thickness and composition of the $\text{Ge}_{1-x}\text{Sn}_x$ layer.

As a first step, this relaxation of the underetched microdisks is evaluated at room temperature. $\text{Ge}_{1-x}\text{Sn}_x$ alloys keep the cubic structure and symmetry.^[31] For this, the stiffness tensor presents only three independent components C_{11} , C_{12} , and C_{44} in the [100], [010], and [001] reference system (using the reduced notation). Reference values for elastic parameters are used for Ge^[14] while for $\text{Ge}_{1-x}\text{Sn}_x$ are linearly interpolated with respect to Sn content, as listed in **Table 2**, and are set as input parameters for the mechanical simulations.

The 3D calculations take into account the $\text{Ge}_{1-x}\text{Sn}_x$, the Ge pedestal, and the Si substrate, reproducing the inset of Figure 1a. The fixed constraint is imposed on the bottom of the Si layer, while $\text{Ge}_{1-x}\text{Sn}_x$ and Ge pedestal are free to expand.

Table 2. Material parameters of Ge^[55] and Sn^[56] used to interpolate the values in their alloy.

Material	Ge	Sn
Density [kg m ⁻³]	5323	5765
Heat capacity [J (kg * K) ⁻¹]	310	213
Thermal conductivity [W (m * K) ⁻¹]	58	63.2
Coefficient of thermal expansion at room T [1/K] (listed for room temperature)	5.9×10^{-6}	5.4×10^{-6}
Relative permittivity	16.3	24
Young's modulus [GPa]	103	50
Poisson's ratio	0.26	0.36
C_{11} [GPa]	122.35	59
C_{12} [GPa]	43	28
C_{44} [GPa]	39.68	26

The relaxation of the layer is estimated selecting as initial conditions the strain reported in Table 1 for $\text{Ge}_{1-x}\text{Sn}_x$ (with $\epsilon_{zz} = -2 \frac{C_{12}}{C_{11}} \epsilon_{bi}$) that corresponds to the one measured by Raman spectroscopy in the center of the microdisk. As initial condition on the domain of the Ge pedestal, a tensile strain of 0.23% is considered. This corresponds to the thermal strain between Ge and the Si substrate after cooling down from growth temperature.^[32]

More details on the strain tensor are reported in the last section of the article and in the appendix.

Having set the numerical model for room temperature, we were also able to extrapolate the strain field at lower temperatures, considering the difference in the coefficients of thermal expansion of Ge and $\text{Ge}_{1-x}\text{Sn}_x$ with respect to silicon, using temperature-dependent values^[33] in the Solid Mechanics model of COMSOL.

3. Results and Discussion

3.1. Strain Analysis

Figure 1a,b shows that the strain landscape obtained by FEM simulations is in good agreement with Raman experimental data. The intensity of the strain field is decreasing going from the center to the periphery. At the center, supported by the pillar, there is a plateau of compressive strain $\epsilon \approx -0.37\%$. On the elastically relaxed rim, there is another plateau with $\epsilon \approx -0.1\%$. The FEM simulation of that region is calculating mechanical deformation for complete elastic relaxation in an ideal sample. In a real microstructure, additional effects, such as nonperfect surfaces and sidewalls or the influence of structural defects (dislocations),^[34] may limit the elastic relaxation. This residual compressive strain remaining on the rim of the disk even after full underetching can be seen on the plots of Figure 1. Comparing a disk with 60 μm diameter (Figure 1a) and one of 20 μm diameter (Figure 1b), we can observe that the size of the microdisk is strongly impacting the strain uniformity (i.e., bigger disks have a wider uniformly strained region). Figure 1b displays also the displacement of thick and thin disk with 10% Sn (dashed lines), finding that thinner disks present a more pronounced bending.

The simulation results show a spike at a distance of 5 μm from the disk's outer edge. This corresponds to the discontinuity between the part of the disk supported by the pedestal and the rim, which is free to expand and thus bends. As we will see in the following sections, this impacts the band structure landscape.

Figure 1c shows a map of the in-plane strain within one of the microdisks obtained by SXDM. The results of this technique fully support both the Raman measurements and the simulations, showing the elastic relaxation of strain on the rim of the disk.

Finally, Figure 1d shows simulated and experimental (Raman) strain profiles at low temperature. The effect of cooling by about around 180 K is translated into an additional tensile biaxial strain of around 0.1% in the center of the disks, while the relaxed area is less affected by thermomechanical effects because the $\text{Ge}_{1-x}\text{Sn}_x$ is not anymore in contact with the Ge and Si substrate and thus free to contract.

3.2. Optical Properties: PL

Disks of 20 and 120 μm radius were measured with micro-PL for each sample in Table 1 in their center, suspended edge, and half-way (for the 120 μm disks where the spot and disk sizes allowed). All the Sn concentrations in our investigation are above the threshold value of 8 at% which allows to consider $\text{Ge}_{1-x}\text{Sn}_x$ a direct bandgap material. From the literature,^[16] it is known that unstrained $\text{Ge}_{0.92}\text{Sn}_{0.08}$ and higher concentrations exhibit direct band alignment. Our model predicts that this holds true for disk Sn8.5, even with the small residual compressive strain measured on its rim. Thus, all the spectra were analyzed with van Roosbroeck's fit^[35] for direct transition in semiconductors (see SI, Supporting Information and ref. [36], for the alternatives to that model):

$$R = A\sqrt{E - E_g}e^{E - E_g/kT_e} \quad (3)$$

where the recombination R is proportional to the product between the thermal occupation of the bands ($e^{E - E_g/kT_e}$) and the joint density of states ($\sqrt{E - E_g}$), where E is the photon energy, E_g the energy gap, and T_e the electronic temperature, while A is an amplitude factor proportional to the transition probability. The electronic temperature can be significantly different from the lattice temperature because of the nonequilibrium conditions under light excitation.^[14] As an example, in the disk Sn8.5 with the size of 20 μm we extracted an electronic temperature of 170 K for a lattice temperature of 80 K.

Figure 2a shows two spectra, measured in the center of the disk Sn8.5, the size of 120 μm , at 81 and 161 K, together with their van Roosbroeck's fit. The high-energy side of the peak is mainly driven by the thermal distribution of carriers and is in good agreement with the fitting procedure. The low-energy part is broadened with respect to the theoretical fit, as a result of limited band filling, indicating a low carrier injection regime,^[37] or alloy broadening and strain inhomogeneity caused by the misfit dislocations at heterointerface,^[38] or localized states extending in

the bandgap to form an Urbach tail,^[39] or also Γ -L recombination.^[14] Moreover, especially for small microdisks, the low-energy tail may be influenced by the spatially dependent radiative recombination. As explained in ref. [14], the excess carrier diffusion length is of the order of μm and the recombination rate may be stronger at the periphery of the disks, where the bandgap is smaller.

The peak shifts to lower energy as the temperature increases, following the typical trend for semiconductors that is empirically described by the formula proposed by Varshni^[40] and widely investigated in the literature:^[41-45]

$$E_g(T) = E_g(0) - \frac{\alpha T^2}{\beta + T} \quad (4)$$

Here, $E_g(0)$ is the bandgap value at $T = 0$ K, while α is related to the electron-phonon coupling, and β is related to the Debye temperature. After having extracted the gap values with Equation 3 for all the samples under investigation, we plotted their behavior as a function of temperature, observing a good alignment with the proposed function in Equation 4 as shown in Figure 3a.

The PL peak (and thus the bandgap) shifts to lower energy as the Sn increases (Figure 2b), in agreement with the literature.^[46-48] Extending the temperature-dependent gap analysis (Equation (3)) for samples with different amounts of Sn, the parameters α and β , as suggested by prior studies,^[47] are not significantly influenced by the Sn concentration in the investigated range (see SIII, Supporting Information and refs. [49,50]). Their values are generally in line with the values extracted for pure Ge, with $\beta = 296 \pm 20$ K and $\alpha = (5.82 \pm 0.4) \cdot 10^{-4}$ eV K⁻².

On the other hand, the amount of Sn is highly impacting the $E_g(0)$ term of Equation (4). Our analysis finds a linear dependence on the Sn content x in range between 8.5% and 14%:

$$E_g(0) = (0.78 \pm 0.003) - (2.07 \pm 0.5) \cdot x \text{ [eV]} \quad (5)$$

Figure 3b shows the behavior of the energy gap as a function of Sn content at room temperature. Our extrapolated results (red

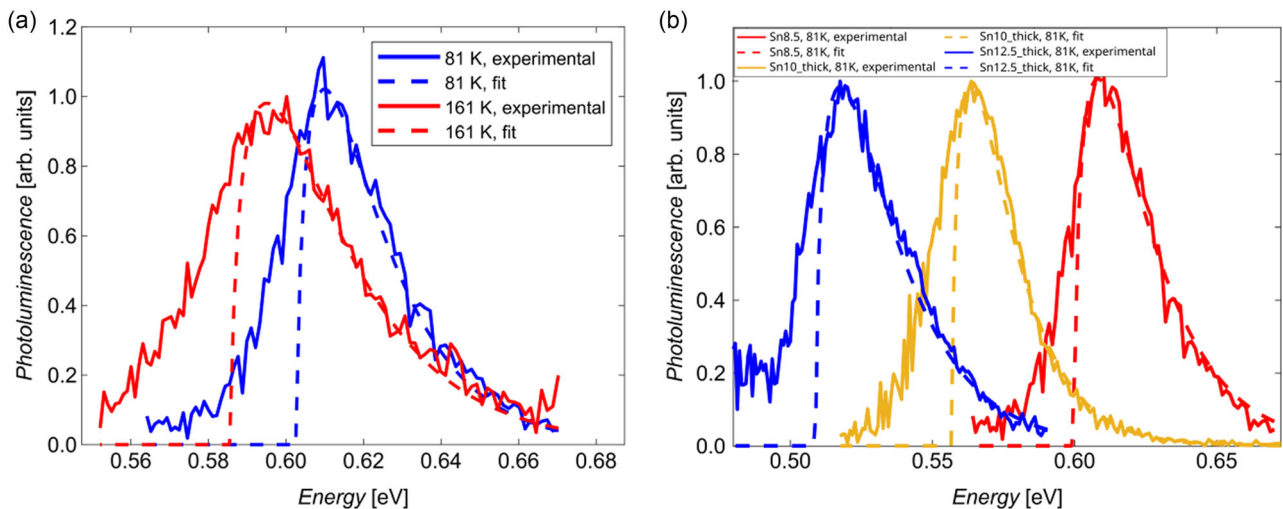


Figure 2. a) PL spectra of sample Sn8.5 at 81 and 161 K, fitted with the van Roosbroeck Equation (3) and normalized for clarity. b) Normalized PL spectra at 81 K for different samples (Sn8.5, Sn10_thick, Sn12.5_thin).

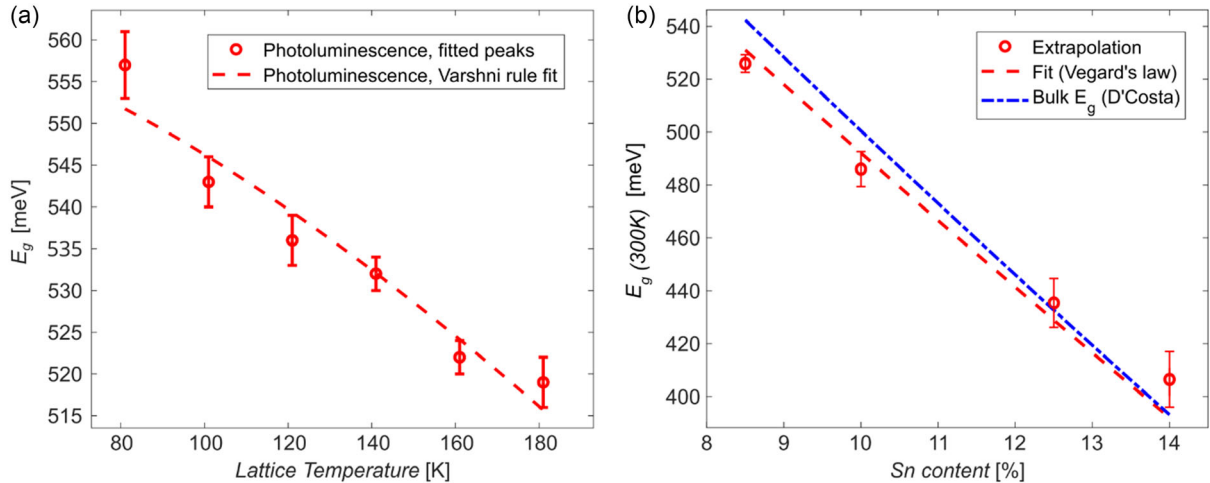


Figure 3. a) An example of Varshni rule fit of the peak positions for the sample Sn12.5_thick. b) A comparison of literature^[46] estimations of E_g at 300 K with the value calculated from the analysis reported in the text for the thickest samples of all the available concentrations in Table 1.

dots) are obtained from Equation (4) with the assumption of α and β as constant values. They present a good agreement with the results of D'Costa et al.^[46] that parametrize E_g as a quadratic function of x :

$$E_{g\text{GeSn}} = E_{g\text{Ge}}(1 - x) + E_{g\text{Sn}}x - bx(1 - x) \quad (6)$$

where b is the bowing parameter, corresponding to 2.46 eV. The value of $E_{g\text{Sn}}$ is taken as -0.41 eV due to the inversion of the Γ_7 and Γ_8 bands in Sn. Also, $E_{g\text{Sn}}$ is expected to change with temperature as described by Equation (4). Alternative descriptions based on interpolation of the Varshni formula are also reported.^[48]

To properly disentangle the effect of strain and Sn on the bandgap, we analyzed the differences between PL spectra at the center and the periphery of the microdisk, reported in Figure 4a for the sample Sn8.5 with disks size of $20 \mu\text{m}$.

The peaks of the two curves are located at different energies, a discrepancy anticipated due to the varying strain profiles.

However, these peaks are not mere rigid shifts from each other, as evidenced by their distinct high energy tails. This variation can be attributed to the spatially dependent laser heating on the microdisk surface. Furthermore, the peak in the edge experimental curve (blue), located at 0.57 eV, may result from noise, a conclusion supported by its absence in other datasets.

The temperature dependence of the bandgap on the rim and the center of the microdisk is shown in Figure 4b. The fit of the experimental data is in line with Equation (4), and the α and β parameters are left unchanged with respect to the previous analysis. The different strain between the center and rim gives a rigid shift of 25 meV between the two curves. This lets us to conclude that the strain is not impacting α and β but only the $E_g(0)$ parameter, as we previously observed for pure Ge.^[14] The energy shift due to strain can be calculated analytically,^[51,52] and confirms the measured value for a measured difference in strain of 0.28%.

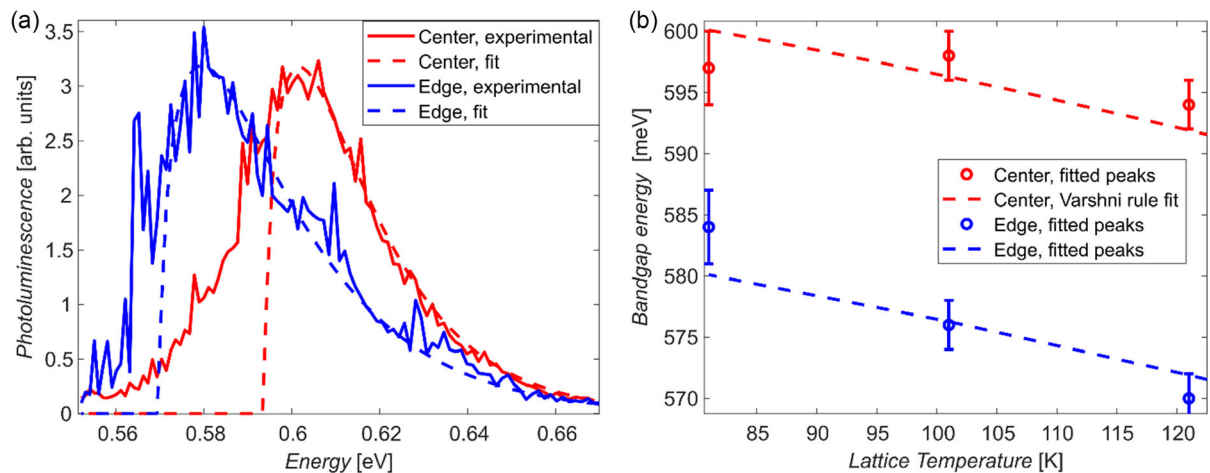


Figure 4. PL in a microdisk with 8.5% Sn in the center and at its edge. a) Comparison between the spectra at 121 K, with the peaks fitted by van Roosbroeck's fit. b) Experimental temperature-dependent peak positions (symbols) and fit with Varshni rule.

4. Thermomechanical Simulations on the Bandgap

The extracted interplay between concentration and strain on the temperature-dependent bandgap became part of our FEM calculation platform that includes the mechanical and thermomechanical relaxation, calculated for the parameters of all of the available samples interpolated from the values listed in Table 2.

As explored in the previous section, we could parametrize, as a result of the experimental analysis, the concentration-dependent bandgap. In addition, our calculations include the strain-dependent valence (Bir and Pikus Hamiltonian^[53,54]) and conduction band (deformation potential theory^[54]) calculations. This approach, first validated with the experimental PL measurements shown in Figure 4 for different strain and positions in the disk, allows us to obtain the band behavior throughout the entire set of the microdisks.

Given the geometry of the system, it is convenient to use cylindrical coordinates. Note, however, that cartesian coordinates, aligned with the crystal axes, are typically used in the calculation of band structure. Because of the change of coordinates, the interpretation of strain and stress tensors components may

differ. We discuss the impact of the off-diagonal components on the band structure in the supplementary.

In order to fully capture the relaxation mechanisms of the system and the impact of the symmetry on the mechanical deformation, we observed the strain components along two different line cuts: one parallel to the x -axis ($\vartheta = 0$), i.e., the (010) direction of the cubic lattice (Figure 5a), and one at 45 degrees with respect to the x -axis ($\vartheta = \pi/4$), i.e., the (100) direction (Figure 5b).

As expected from the cylindrical symmetry of the system,^[12] the ϵ_{xx} and ϵ_{yy} components are not equal to each other in all the points of the disk, as well as ϵ_{rr} and $\epsilon_{\varphi\varphi}$. At specific positions, e.g., along the line cut at $\vartheta = 0$ of Figure 5a, the off-diagonal components are entirely negligible in both the coordinate systems and $\epsilon_{xx} = \epsilon_{rr}$ and $\epsilon_{yy} = \epsilon_{\varphi\varphi}$. On the other hand, a line cut at $\vartheta = \pi/4$ shows the strong contribution of the off-diagonal components in the cartesian coordinates. In Figure 5c, we report our theoretical calculations for the band edge profiles of heavy hole (HH) and light hole (LH) bands evaluated employing the Bir-Pikus Hamiltonian and providing as input the strains obtained with COMSOL Multiphysics, showing how the band edge profile is invariant with respect to the choice of the coordinate system, as expected.

Figure 6a shows the bandgap along the disk, with the expected radial symmetry. In this case, as in Figure 6b, the strain-

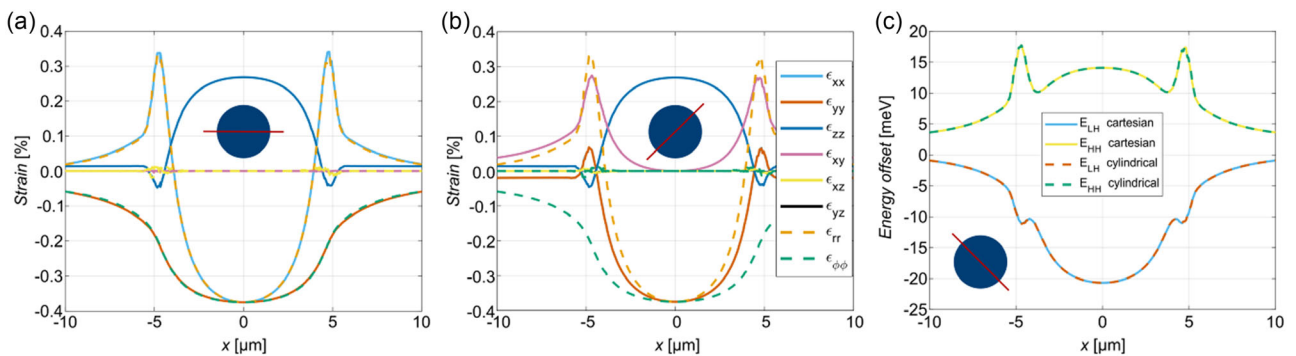


Figure 5. a) Strain components in cylindrical coordinates and in cartesian coordinates along a line cut on the horizontal axis ($\vartheta = 0$) and 10 nm below the surface; b) strain components in cylindrical coordinates and in cartesian coordinates along a line cut oriented at 45 degrees with respect to the x -axis ($\vartheta = \pi/4$) and 10 nm below the surface; c) HH band profile (green) and LH band profile (blue) along the horizontal line cuts of respectively. The continuous lines are extracted in cartesian coordinates, the dashed in cylindrical.

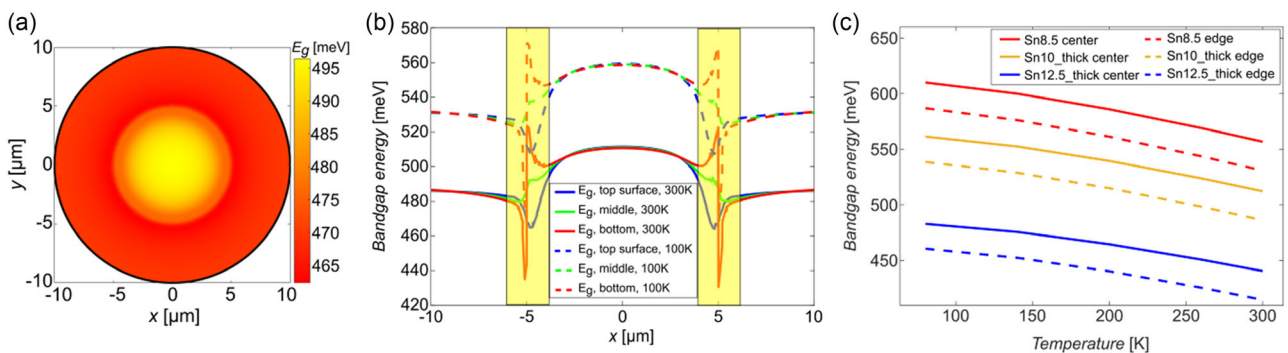


Figure 6. a) Color map of the energy gap extracted 2 nm below the surface; b) energy gap profiles extracted along the horizontal line cut at room T (continuous lines) and 100 K (dashed lines) at the top (blue), middle (green), and bottom (red) of the disk; c) energy gap as a function of temperature for 8.5% Sn concentration (red), 10% Sn concentration (green), and 12.5% Sn concentration (blue) on the center (continuous) or the edge (dashed) of the microdisk.

dependent variation of the HH valence band is obtained following the full diagonalized approach.^[52] In contrast, the conduction band offset only depends on the hydrostatic strain and is not influenced by off-diagonal components.^[54] Along the entire surface of the disk, the strain-induced energy variation of the gap ranges in an interval of 30 meV.

Figure 6b illustrates the behavior of the horizontal line cut of the band energy gap for room temperature (continuous lines) and 100 K temperature (dashed lines). Cooling down the sample causes a rigid increase of the energy gap of more than 40 meV. As observed in the section dedicated to mechanical deformations, the simulation results show a spike at a distance of 5 μm from the outer edge of the disk (area highlighted in yellow). This region corresponds to the interface between the part of the disk supported by the pedestal (and thus constrained by the Ge) and the rim that is free to expand. In this region, the mechanical deformation also has a strong gradient along the vertical direction. As observed from the red, blue, and green curves of Figure 6b, showing, respectively, line cuts along the x -axis at the bottom, top, and middle of the microdisk, the energy bandgap can vary in a range of more than 50 meV, strongly impacting the radiative and nonradiative recombination mechanism as also already observed for different structures.^[14] For the case of the top surface of the disk, we can conclude that the difference between the minimum of the energy gap in the interface region and the energy gap at the rim is around 20 meV, i.e., comparable temperature effect and composition effect.

To obtain a complete description of the spatially dependent bandgap, we use the modeling and parameterization of the temperature dependence for strain and bandgap developed in the previous sections, together with the composition effect. The effect of strain has been included, in its effect on the bandgap at $T = 0$ K, i.e., the $E_g(0)$ of the Varshni relation, with the contributions to it including both lattice mismatch and thermal strain, the latter of which is normally contributing to the Varshni parameters listed in literature. Together with the dependence of the band structure on Sn content and temperature, a full parameterization is achieved.

The main findings are summarized in Figure 6c. The continuous lines are showing the behavior of the energy gap as a function of the temperature in the center of the microdisk, the dashed at the periphery. As commented above, the difference of strain between center and rim results in a shift of the bandgap comparable with that of the temperature in 100 K range. Note that in optically pumped devices the local electronic temperature can increase by several tens of K with respect to lattice temperature, as noted from the Roosbroeck's fit in Figure 2. Thus, the alignment of the band edge along the disk can be severely altered from the one predicted in equilibrium conditions.

The influence of the three main parameters—temperature T , Sn content x , and strain ϵ —is described by our model. As a benchmark, we estimate the slopes of the 1D curves $E(T)$, $E(x)$, $E(\epsilon)$ obtained from the bandgap $E(T, x, \epsilon)$ parameterized for our microdisks by keeping the other parameters fixed. For one exemplary disk (Sn10_thick, in the case used for the illustrations in this section), they are obtained as $\frac{dE}{dT} \cong 0.43 \frac{\text{meV}}{\text{K}}$,

$\frac{dE}{dx} \cong 31.7 \frac{\text{meV}}{1\% \text{ Sn}}$, and $\frac{dE}{d\epsilon} \cong 7.85 \frac{\text{meV}}{10^{-3}}$, respectively. This range of bandgap variations dependent on different factors shows the importance of a complete thermomechanical description for optoelectronic-based devices.

5. Conclusions

We give a parametrization of the bandgap in $\text{Ge}_{1-x}\text{Sn}_x$ devices depending on Sn content, temperature, and the spatial strain distribution, including shear strain, using a self-calibrated theoretical/experimental tool among Raman spectroscopy, XRD, PL, and FEM simulations. The elastic relaxation mechanism is fully described by combining FEM calculations and Raman spectroscopy for different Sn concentrations and temperatures. This approach offers a 3D calculation of the strain profiles and strain gradients in a wide range of temperatures.

To fully determine the influence of mechanical and thermo-mechanical features on optical properties, we analyze temperature-dependent PL spectra with strain-dependent Bir-Pikus Hamiltonian and Van Roosbroeck fitting. Moreover, we use the combination of the abovementioned models to describe the temperature-dependent bandgap, parametrizing the interaction between strain, Sn content, and temperature. The contributions of those parameters are, respectively, described by the strain-dependent Bir-Pikus Hamiltonian (with a typical drop of 20 meV for the bandgap on the relaxed edge), Vegard's law for composition (around 20 meV decrease per 1% Sn in the measured range of compositions), and empirical Varshni rule for temperature (with an example drop from 555 meV at 81 K to 520 meV at 181 K). An additional dip of ≈ 20 meV caused by the bending at the edge of the pillar could result in a shift of up to 50 nm in the normal GeSn emission wavelength of $\approx 2.5 \mu\text{m}$ at the abovementioned operating temperature ranges for our microdisks, depending on the exact location of the modes. This highlights the importance of comprehensive modeling for the strained microstructures.

As a result of our work, we offer an insight for assessing integrated light emitters designed to work at cryogenic temperatures or in presence of high power. In this framework, the knowledge of the interplay between the key role played by temperature, strain, and Sn concentration would be very beneficial to the advancement of this technology.

Supporting Information

Supporting Information is available from the Wiley Online Library or from the author.

Acknowledgements

I.Z. and A.A.C.-W. contributed equally to this work. The authors acknowledge Dr. Dan Mihail Buca from Peter Grünberg Institute (PGI), Forschungszentrum Jülich for providing the samples and Prof. Giovanni Capellini for the useful discussion. B.M.-G. thanks the support from Agencia Estatal de Investigación - Ministerio de Ciencia e Innovación (Spain) grant: "Ramón y Cajal fellowship" (grant no. RYC2021-034836-I). C.L.M. and I.Z. thank the fruitful

discussion with Dr. Marco Salvalaglio from the Technische Universität Dresden. The authors acknowledge the European Synchrotron Radiation Facility (ESRF) for provision of synchrotron radiation facilities.

Open Access funding enabled and organized by Projekt DEAL.

Conflict of Interest

The authors declare no conflict of interest.

Data Availability Statement

The data that support the findings of this study are available from the corresponding author upon reasonable request.

Keywords

band structures, $\text{Ge}_{1-x}\text{Sn}_x$, photoluminescence, Raman, semiconductors, strains

Received: September 1, 2023

Revised: October 23, 2023

Published online: November 20, 2023

- [1] C. L. Senaratne, P. M. Wallace, J. D. Gallacher, P. E. Sims, J. Kouvetakis, J. Menéndez, *J. Appl. Phys.* **2016**, *120*, 025701.
- [2] Y. Zhou, W. Dou, W. Du, S. Ojo, H. Tran, S. A. Ghetmiri, S.-Q. Yu, *ACS Photonics* **2019**, *6*, 1434.
- [3] Z. Zhou, X. Ou, Y. Fang, E. Alkharaji, R. Xu, Y. Wan, J. E. Bowers, *eLight* **2023**, *3*, 1.
- [4] H. Lin, Z. Luo, T. Gu, L. C. Kimerling, K. Wada, A. Agarwal, J. Hu, *Nanophotonics* **2018**, *7*, 393.
- [5] O. Moutanabbir, S. Assali, X. Gong, E. O'Reilly, C. A. Broderick, B. Marzban, J. Witzens, W. Du, S.-Q. Yu, A. Chelnokov, D. Buca, D. Nam, *Appl. Phys. Lett.* **2021**, *118*, 110502.
- [6] J. Chrétien, N. Pauc, F. Armand Pilon, M. Bertrand, Q.-M. Thai, L. Casiez, N. Bernier, H. Dansas, P. Gergaud, E. Delamadeleine, R. Khazaka, H. Sigg, J. Faist, A. Chelnokov, V. Reboud, J.-M. Hartmann, V. Calvo, *ACS Photonics* **2019**, *6*, 2462.
- [7] J. Margetis, S. Al-Kabi, W. Du, W. Dou, Y. Zhou, T. Pham, P. Grant, S. Ghetmiri, A. Mosleh, B. Li, J. Liu, G. Sun, R. Soref, J. Tolle, M. Mortazavi, S.-Q. Yu, *ACS Photonics* **2018**, *5*, 827.
- [8] R. Soref, *Nat. Photonics* **2010**, *4*, 495.
- [9] S. Gupta, B. Magyari-Köpe, Y. Nishi, K. C. Saraswat, *J. Appl. Phys.* **2013**, *113*, 073707.
- [10] Y. Chibane, M. Ferhat, *J. Appl. Phys.* **2010**, *107*, 053512.
- [11] D. Buca, A. Bjelajac, D. Spirito, O. Concepción, M. Gromovyi, E. Sakat, X. Lafosse, L. Ferlazzo, N. von den Driesch, Z. Ikonik, D. Grützmacher, G. Capellini, M. El Kurdi, *Adv. Opt. Mater.* **2022**, *10*, 2201024.
- [12] D. Stange, S. Wirths, R. Geiger, C. Schulte-Braucks, B. Marzban, N. von den Driesch, G. Mussler, T. Zabel, T. Stoica, J.-M. Hartmann, S. Mantl, Z. Ikonik, D. Grützmacher, H. Sigg, J. Witzens, D. Buca, *ACS Photonics* **2016**, *3*, 1279.
- [13] A. Elbaz, D. Buca, N. von den Driesch, K. Pantzas, G. Patriarache, N. Zerounian, E. Herth, X. Checoury, S. Sauvage, I. Sagnes, A. Foti, R. Ossikovski, J.-M. Hartmann, F. Boeuf, Z. Ikonik, P. Boucaud, D. Grützmacher, M. El Kurdi, *Nat. Photonics* **2020**, *14*, 375.
- [14] C. L. Manganelli, M. Virgilio, M. Montanari, I. Zaitsev, N. Andrioli, S. Faralli, S. Tirelli, F. Dagnano, W. M. Klesse, D. Spirito, *Phys. Status Solidi A* **2021**, *218*, 2100293.
- [15] H. Lin, R. Chen, Y. Huo, T. Kamins, J. Harris, *Appl. Phys. Lett.* **2011**, *98*, 261917.
- [16] S. Wirths, R. Geiger, N. von den Driesch, G. Mussler, T. Stoica, S. Mantl, Z. Ikonik, M. Luysberg, S. Chiussi, J.-M. Hartmann, H. Sigg, J. Faist, D. Buca, D. Grützmacher, *Nat. Photonics* **2015**, *9*, 88.
- [17] V. Reboud, A. Gassenq, N. Pauc, J. Aubin, L. Milord, Q. M. Thai, M. Bertrand, K. Guillo, D. Rouchon, T. Zabel, F. A. Pilon, H. Sigg, A. Chelnokov, J. M. Hartmann, V. Calvo, *Appl. Phys. Lett.* **2017**, *111*, 5.
- [18] Q. M. Thai, N. Pauc, J. Aubin, M. Bertrand, J. Chrétien, V. Delaye, V. Calvo, *Opt. Express* **2018**, *26*, 32500.
- [19] S. Amoah, S. Ojo, H. Tran, G. Abernathy, Y. Zhou, W. Du, J. Margetis, J. Tolle, B. Li, S.-Q. Yu, in *Conf. Lasers and Electro-Optics*, Optica Publishing Group, San Jose, CA **2021**, p. SM1H.4.
- [20] S. Ojo, Y. Zhou, S. Acharya, N. Saunders, S. Amoah, Y.-T. Jheng, H. Tran, W. Du, G.-E. Chang, B. Li, S.-Q. Yu, in *Physics and Simulation of Optoelectronic Devices XXX* (Eds: M. Osinski, Y. Arakawa, B. Witzigmann), SPIE, San Francisco **2022**, p. 15.
- [21] Q. M. Thai, J. Chrétien, M. Bertrand, J. Aubin, L. Casiez, A. Chelnokov, J.-M. Hartmann, V. Reboud, N. Pauc, V. Calvo, *IEEE J. Sel. Top. Quantum Electron.* **2022**, *28*, 1.
- [22] S. Wirths, D. Stange, R. Geiger, Z. Ikonik, T. Stoica, G. Mussler, J.-M. Hartmann, H. Sigg, D. Grützmacher, S. Mantl, D. Buca, in *11th Int. Conf. Group IV Photonics (GFP)*, IEEE, Paris **2014**, pp. 13–14.
- [23] S. Gupta, E. Simoen, R. Loo, Y. Shimura, C. Porret, F. Gencarelli, K. Paredis, H. Bender, J. Lauwaert, H. Vrielinck, M. Heyns, *Appl. Phys. Lett.* **2018**, *113*, 022102.
- [24] G. Zhu, T. Liu, Z. Zhong, X. Yang, L. Wang, Z. Jiang, *Nanoscale Res. Lett.* **2020**, *15*, 18.
- [25] A. Gassenq, L. Milord, J. Aubin, N. Pauc, K. Guillo, J. Rothman, D. Rouchon, A. Chelnokov, J.-M. Hartmann, V. Reboud, *Appl. Phys. Lett.* **2017**, *110*, 112101.
- [26] D. Spirito, N. von den Driesch, C. L. Manganelli, M. Zoellner, A. A. Corley-Wiciak, Z. Ikonik, T. Stoica, D. Grützmacher, D. Buca, G. Capellini, *ACS Appl. Energy Mater.* **2021**, *4*, 7385.
- [27] C. Richter, V. M. Kaganer, A. Even, A. Dussaigne, P. Ferret, F. Barbier, Y.-M. Le Vaillant, T. U. Schüllli, *Phys. Rev. Appl.* **2022**, *18*, 064015.
- [28] C. Corley-Wiciak, M. H. Zoellner, I. Zaitsev, K. Anand, E. Zatterin, Y. Yamamoto, A. A. Corley-Wiciak, F. Reichmann, W. Langheinrich, L. R. Schreiber, C. L. Manganelli, M. Virgilio, C. Richter, G. Capellini, *Phys. Rev. Appl.* **2023**, *20*, 024056.
- [29] F. Gencarelli, B. Vincent, J. Demeulemeester, A. Vantomme, A. Moussa, A. Franquet, A. Kumar, H. Bender, J. Meersschaut, W. Vandervorst, R. Loo, M. Caymax, K. Temst, M. Heyns, *ECS J. Solid State Sci. Technol.* **2013**, *2*, P134.
- [30] L. Kormoš, M. Kratzer, K. Kosteci, M. Oehme, T. Šikola, E. Kasper, J. Schulze, C. Teichert, *Surf. Interface Anal.* **2017**, *49*, 297.
- [31] C. L. Manganelli, P. Pintus, C. Bonati, *Opt. Express* **2015**, *23*, 28649.
- [32] G. Capellini, M. D. Seta, P. Zaumseil, G. Kozłowski, T. Schroeder, *J. Appl. Phys.* **2012**, *111*, 073518.
- [33] R. Roucka, Y.-Y. Fang, J. Kouvetakis, A. V. G. Chizmeshya, J. Menéndez, *Phys. Rev. B* **2010**, *81*, 245214.
- [34] A. Fischer, H. Kühne, M. Eichler, F. Holländer, H. Richter, *Phys. Rev. B* **1996**, *54*, 8761.
- [35] H. Bebb, E. Williams, in *Semiconductors and Semimetals*, Vol. 8 (Eds: R. Williardson, A. C. Beer), Academic Press, New York and London **1972**.

- [36] P. L. Grande, A. Hentz, R. P. Pezzi, I. J. R. Baumvol, G. Schiwietz, *Nucl. Instrum. Methods Phys. Res., Sect. B* **2007**, 256, 92.
- [37] S. Assali, A. Dijkstra, A. Attiaoui, É. Bouthillier, J. E. M. Haverkort, O. Moutanabbir, *Phys. Rev. Appl.* **2022**, 15, 024031.
- [38] S. Assali, A. Dijkstra, A. Attiaoui, É. Bouthillier, J. E. M. Haverkort, O. Moutanabbir, *Phys. Rev. Appl.* **2021**, 15, 024031.
- [39] S. Aljishi, J. D. Cohen, S. Jin, L. Ley, *Phys. Rev. Lett.* **1990**, 64, 2811.
- [40] Y. P. Varshni, *Physica* **1967**, 34, 149.
- [41] K. P. O'Donnell, X. Chen, *Appl. Phys. Lett.* **1991**, 58, 2924.
- [42] A. Manoogian, A. Leclerc, *Phys. Status Solidi B* **1979**, 92, K23.
- [43] T. Donofrio, G. Lamarche, J. C. Woolley, *J. Appl. Phys.* **1985**, 57, 1932.
- [44] L. Vina, S. Logothetidis, M. Cardona, *Phys. Rev. B* **1979**, 30, 1979.
- [45] A. T. Collins, S. C. Lawson, G. Davies, H. Kanda, *Phys. Rev. Lett.* **1990**, 65, 891.
- [46] V. R. D'Costa, C. S. Cook, A. G. Birdwell, C. L. Littler, M. Canonico, S. Zollner, J. Kouvetakis, J. Menéndez, *Phys. Rev. B* **2006**, 73, 125207.
- [47] K. Zelazna, M. Wełna, J. Misiewicz, J. Dekoster, R. Kudrawiec, *J. Phys. D: Appl. Phys.* **2016**, 49, 235301.
- [48] M. Bertrand, Q.-M. Thai, J. Chrétien, N. Pauc, J. Aubin, L. Milord, A. Gassenq, J.-M. Hartmann, A. Chelnokov, V. Calvo, V. Reboud, *Ann. Phys.* **2019**, 531, 1800396.
- [49] L. Viña, S. Logothetidis, M. Cardona, *Phys. Rev. B* **1984**, 30, 1979.
- [50] K. Huang, A. Rhys, *Proc. R. Soc. London, Ser. A* **1950**, 204, 406.
- [51] M. Virgilio, C. L. Manganeli, G. Grosso, G. Pizzi, G. Capellini, *Phys. Rev. B* **2013**, 87, 235313.
- [52] C. Y.-P. Chao, S. L. Chuang, *Phys. Rev. B* **1992**, 46, 4110.
- [53] G. L. Bir, G. E. Pikus, *Symmetry and Strain-Induced Effects in Semiconductors*, Wiley, New York **1974**.
- [54] C. G. Van de Walle, *Phys. Rev. B* **1989**, 39, 1871.
- [55] *New Semiconductor Materials, Characteristics and Properties 2020*, <http://www.ioffe.ru/SVA/>.
- [56] *Group IV Elements, IV-IV and III-V Compounds. Part B - Electronic, Transport, Optical and Other Properties, Vol. b* (Eds: O. Madelung, U. Rössler, M. Schulz), Springer-Verlag, Berlin/Heidelberg **2002**.